




Cite this: DOI: 10.1039/d5mh01137j

Received 16th June 2025,
Accepted 7th August 2025

DOI: 10.1039/d5mh01137j

rsc.li/materials-horizons

Enhancing oxygen evolution reaction performance *via* Zn/Fe co-doping in a Co₃O₄ nanostructure: mechanistic insights and surface reconstruction dynamics

Qianwen Chen,^a Yanbing Huang,^a Wanshun Duan,^a Qijia Su,^a Yilong Wang,^a
Fuxi Bao,^a Junjun Zhang ^{*b} and Wen Guo^{*a}

The kinetics of the oxygen evolution reaction (OER) of Co₃O₄ in alkaline media can be promoted by a bimetallic co-doping strategy. Herein, we synthesize a Zn/Fe co-doped Co₃O₄ nanostructure (ZnFe–Co₃O₄) to enhance the oxygen evolution reaction performance in alkaline media. The ZnFe–Co₃O₄ electrocatalyst exhibits a low overpotential of 255 mV at 10 mA cm^{−2}, a Tafel slope of 54 mV dec^{−1} in 1.0 M KOH and excellent long-term durability of up to 120 hours at 100 mA cm^{−2}. X-ray photoelectron spectroscopy (XPS) reveals that Zn occupies octahedral Co³⁺ sites and Fe occupies tetrahedral Co²⁺ sites in the Co₃O₄ lattice. The experimental results together with theory calculations collectively demonstrate that ZnFe–Co₃O₄ follows the lattice oxygen mechanism (LOM) during the OER process. *In situ* Raman spectroscopy shows that truly active FeOOH/CoOOH species are formed through surface reconstruction during the OER. Furthermore, it is found that the synergistic effects of Zn and Fe doping, which stabilize the Co₃O₄ structure and promote the generation of active (oxy)hydroxide species, are identified as key factors in enhancing the electrocatalytic performance. This work offers a novel concept for enhancing the electrocatalytic activity of electrocatalysts through doping strategies and provides guidance for the rational design of ideal electrocatalysts.

New concepts

Alkaline water electrolysis technology powered by renewable solar and wind energy is an effective method for producing green hydrogen, which is critical for reducing carbon emissions. Developing high-performance electrocatalysts to enhance water splitting is key to improving hydrogen production through water electrolysis. Herein, we combine PA etching and heteroatom doping using ZIFs as a precursor to construct a Zn/Fe co-doped Co₃O₄ architecture (ZnFe–Co₃O₄). The electrocatalyst exhibits high OER activity and long-term durability during the water splitting process. Various *in situ* and other techniques revealed that the electrocatalyst is converted into (oxy)hydroxide species (*i.e.*, FeOOH/CoOOH) on the surface, which serve as the true active sites for the electrocatalytic process. Additionally, the distinct roles of Zn and Fe atoms in the OER process are also elucidated: Zn atoms stabilize the Co₃O₄ structure to some extent, while Fe atoms facilitate the generation of highly active (oxy)hydroxide species. Meanwhile, the combination of electrochemical, multiple *in situ* characterization and DFT collectively demonstrates that the electrocatalyst follows the LOM pathway. The findings highlight the importance of synergistic doping and surface reconstruction in optimizing the electrocatalytic properties of Co₃O₄-based materials, paving the way for the development of more efficient and durable OER electrocatalysts.

1 Introduction

The depletion of fossil fuels (coal, natural gas and oil) has caused energy shortages and environmental problems, spurring the development of sustainable energy sources such as solar, wind and tidal power.¹ However, the intermittent nature of sustainable energy sources, which is affected by factors such as the time

of day, weather and geographical location, significantly limits their practical applications. The conversion of sustainable energy into chemical energy has proven to be an effective and promising approach to solving the above problem. Due to its zero emissions and wide availability, hydrogen, with a specific gravimetric energy density of 142 MJ kg^{−1}, has attracted great attention as an important energy vector.² Of the technologies used to produce hydrogen, photovoltaic-driven electrochemical water splitting (PV-EC) is particularly appealing because both photovoltaics and water splitting are well-established technologies.^{3–6} However, the low rate of hydrogen production in water splitting due to the slow kinetics of the oxygen evolution reaction (OER) at the anode severely limits the development of PV-EC technology.^{7–10} For this reason, a great deal of effort has been made to develop highly efficient OER electrocatalysts in recent years.¹¹ Noble metal materials, such as RuO₂ and IrO₂, have so far been shown to be the most effective electrocatalysts

^a School of Chemistry and Chemical Engineering/State Key Laboratory Incubation Base for Green Processing of Chemical Engineering, Shihezi University, Shihezi, 832003, China. E-mail: wenguo@shzu.edu.cn

^b State Key Laboratory of High-Efficiency Utilization of Coal and Green Chemical Engineering, College of Chemistry and Chemical Engineering, Ningxia University, Yinchuan, Ningxia, 750021, China. E-mail: zhangjj089@nxu.edu.cn

for the OER.¹² However, their large-scale exploration is largely limited by their scarcity and preciousness.¹³

Transition metal-based materials have been explored as OER electrocatalysts due to their satisfactory activities and durability, especially in alkaline media.^{14,15} Cobalt-based materials are one of the main types of materials being developed for the OER due to their unsaturated 3d electronic tenable chemical valence, abundant crustal reserves and good stability in electrolytes.^{16,17} However, cobalt-based electrocatalysts have problems of poor conductivity and a single active site, and the introduction of metal ions can overcome these shortcomings, thereby improving OER performance.^{18–20} For example, Zhang *et al.* prepared Mo-substituted and oxygen vacancy enriched hierarchical spinel Co_3O_4 porous nanoneedle arrays on carbon cloth (P-Mo- Co_3O_4 @CC) by a simple and effective Ar-plasma-assisted method. They found that the incorporation of Mo atoms produces more electrocatalytically active sites and optimizes the electronic structure of Co sites by combining oxygen vacancies with Mo atom doping.²¹ Consequently, the introduction of appropriate alien metal atoms into the crystal lattice of Co_3O_4 is anticipated to bolster its electrocatalytic OER activity.

Zeolitic imidazolate frameworks (ZIFs), a subclass of metal-organic frameworks (MOFs), are characterized by a zeolite-like topological structure and are composed of the coordination of metal ions and 2-methylimidazole ligands.²² ZIFs have garnered attention as a promising material for fabricating OER electrocatalysts due to their high porosity structure, large specific surface area and excellent chemical stability.^{23,24} Nevertheless, pristine ZIFs face several challenges, including poor conductivity and electrocatalytic performance.²⁵ The existing strategies are mainly to obtain ZIF-derived materials through high-temperature pyrolysis to enhance the conductivity of the electrocatalyst and improve the electrocatalytic performance.^{26,27} However, high-temperature pyrolysis can lead to structural collapse, which may negate the advantages of high porosity and large surface area that ZIFs are known for.²⁸ Therefore, it is a great challenge to maintain the structure and morphology of ZIFs themselves, to fully utilize their porous advantages, to significantly increase the number of active sites, and to improve their conductivity. Recently, Zhang *et al.* used ZIF-67 as a precursor to construct a phytic acid (PA) cross-linked cobalt-based complex ($\text{Co}(\text{Fe})\text{-PA}$), which could be rapidly and completely reconstructed under the alkaline OER. They found that PA molecules could be etched into the interior of ZIF-67 to form a hollow porous nanobox, which promotes the penetration of the electrolyte into the inner part of the material, thereby accelerating the reconstruction process.²⁹ Further studies have shown that PA contains six phosphate groups that readily form coordination complexes with transition metals, inhibiting metal polymerization and enabling polymetallic doping.³⁰ In addition, the interaction between PA molecules and transition metals results in the formation of an extensive cross-linking network, which facilitates close spatial proximity between active metal sites, thereby enhancing synergistic electrocatalysis; meanwhile, the hollow structure created by PA etching would expose numerous active sites, facilitating electrolyte penetration and electron/ion migration.^{29,31,32}

In conclusion, the strategy of etching ZIFs by PA can offer prospects for the preparation of electrocatalysts.

Inspired by the above considerations, herein, we combine the PA etching and heteroatom doping using ZIFs as a precursor to construct a Zn/Fe co-doped Co_3O_4 architecture ($\text{ZnFe-Co}_3\text{O}_4$). The $\text{ZnFe-Co}_3\text{O}_4$ electrocatalyst exhibits low overpotentials of only 255 and 380 mV at 10 and 100 mA cm^{-2} , a Tafel slope of 54 mV dec^{-1} in 1.0 M KOH and shows excellent long-term durability of up to 120 hours at 100 mA cm^{-2} . X-ray photoelectron spectroscopy (XPS) reveals the positions of metal atoms in the Co_3O_4 lattice, with Zn atoms occupying octahedral Co^{3+} and Fe atoms occupying tetrahedral Co^{2+} . Theoretical calculations, together with pH-dependent, tetramethylammonium (TMA^+) adsorption, differential electrochemical mass spectroscopy (DEMS) and *in situ* attenuated total reflectance-Fourier transform infrared spectroscopy (ATR-FTIR) measurements, demonstrate that $\text{ZnFe-Co}_3\text{O}_4$ follows the lattice oxygen mechanism (LOM) during the OER. Furthermore, the OER process is monitored by *in situ* Raman spectroscopy, revealing the formation of true highly active FeOOH/CoOOH species through surface reconstruction. The different roles of Zn and Fe atoms in the OER process are also elucidated: Zn atoms stabilize the Co_3O_4 structure to some extent, while Fe atoms facilitate the generation of highly active (oxy)hydroxide species. These findings elucidate the underlying mechanisms of enhanced electrocatalytic performance and provide valuable insights for the rational design of advanced electrocatalysts.

2. Experimental section

2.1. Chemicals and materials

2-Methylimidazole ($\text{C}_4\text{H}_6\text{N}_2$, 98%), phytic acid solution ($\text{C}_6\text{H}_{18}\text{O}_{24}\text{P}_6$, 70% in H_2O) and zinc nitrate hexahydrate ($\text{Zn}(\text{NO}_3)_2 \cdot 6\text{H}_2\text{O}$) were purchased from Shanghai Aladdin Biochemical Technology Co., Ltd. Ferric nitrate nonahydrate ($\text{Fe}(\text{NO}_3)_3 \cdot 9\text{H}_2\text{O}$, 98%) was purchased from Shanghai Titan Scientific Co., Ltd. Cobalt nitrate hexahydrate ($\text{Co}(\text{NO}_3)_2 \cdot 6\text{H}_2\text{O}$, 99%), polyvinylpyrrolidone ($(\text{C}_6\text{H}_9\text{NO})_n$, MW:8000, K16-18) and potassium hydroxide (KOH, 90%) were purchased from Shanghai Macklin Biochemical Co., Ltd. All chemicals and reagents were analytically pure and used without further purification.

2.2. Synthesis of ZnCo-ZIF

In a typical procedure, 0.52 mmol $\text{Co}(\text{NO}_3)_2 \cdot 6\text{H}_2\text{O}$ and 0.13 mmol $\text{Zn}(\text{NO}_3)_2 \cdot 6\text{H}_2\text{O}$ were dissolved in 10 mL of deionized water. 6 mmol 2-methylimidazole and 200 mg of PVP were dissolved in 10 mL of deionized water. The two solutions were mixed thoroughly and placed in 3 pieces of Nickel Foam ($1 \times 3 \text{ cm}^2$) and left at room temperature for 10 hours.

2.3. Synthesis of ZnCo-PA and Fe-ZnCo-PA

ZnCo-ZIF was first dispersed in 50 mL of ethanol containing 100 mg of PVP, and then 15 mL of ethanol/PA mixed solvent ($V_{\text{ethanol}}/V_{\text{PA}} = 40:1$) was added. The solution was stirred at room temperature for 60 min.

2.4. Synthesis of Fe–ZnCo–PA

121.2 mg of $\text{Fe}(\text{NO}_3)_3 \cdot 9\text{H}_2\text{O}$ was mixed with 10 mL of water and ZnCo–PA was left in solution for 5 min at room temperature.

2.5. Synthesis of ZnFe–Co₃O₄

Fe–ZnCo–PA was calcined at 300 °C for 3 hours in air with a heating rate of 5 °C min^{−1} and cooled down naturally.

2.6. Materials and characterization

The microstructures of all samples were measured using a field emission scanning electron microscope (SEM, ZEISS Sigma 300) and a transmission electron microscope (TEM, FEI Talos F200x). Energy-dispersive spectroscopy (EDS) was used to investigate the elemental content and mapping of the ZnFe–Co₃O₄ sample. To characterize the phase structure of the samples, X-ray diffraction (XRD) patterns were collected using a Rigaku SmartLab SE from 5° to 90° at a rate of 5° min^{−1}. Raman spectroscopy (Bruker; $\lambda = 785 \text{ nm}$) was applied to obtain the vibronic response of the samples. The chemical states and electronic structures of the samples were analysed by X-ray photoelectron spectroscopy (XPS) on a Thermo Scientific K-Alpha and the binding energies were calibrated using the C 1s peak at 284.8 eV. An inductively coupled plasma optical emission spectroscopy (ICP-OES) test was conducted on an Agilent 700.

2.7. Electrochemical measurements

All electrochemical measurements were performed in 1.0 M KOH (pH = 14.0) electrolyte at room temperature using an electrochemical workstation (CHI 760E, Shanghai, China). In the three-electrode mode, nickel foam (size: 1 × 1 cm²) containing active materials, a Hg/HgO electrode and a graphite rod acted as the working, reference and counter electrodes, respectively.

All recorded electrode potentials were calibrated to reversible hydrogen electrode (*vs.* RHE) potentials using eqn (1):

$$E_{\text{RHE}} = E_{\text{Hg/HgO}} + 0.059 \times \text{pH} + 0.098 \text{ V} \quad (1)$$

where E_{RHE} refers to the reversible hydrogen electrode potential and the $E_{\text{Hg/HgO}}$ refers to the electrode potential of the Hg/HgO electrode.

The voltametric curves of the OER were recorded using the linear sweep voltammetry (LSV) technique at a scan rate of 2 mV s^{−1}. All the LSV curves were calibrated using 100% iR-compensation.

The EIS data were collected in the frequency range of 100 KHz to 0.01 Hz with a perturbation amplitude of 5 mV at 0.65 V *vs.* Hg/HgO for the OER.

The double-layer capacitance (C_{dl}) values of the as-prepared electrocatalysts were determined using a typical cyclic voltammetry (CV) method. The CV data for the OER were recorded in a potential range of −0.112 to −0.102 V *vs.* Hg/HgO, with scan rates ranging from 20, 40, 60, 80 and 100 mV s^{−1}.

The electrochemically active surface area (ECSA) could be calculated as follows:

$$\text{ECSA} = S_{\text{geo}} \times \frac{C_{\text{dl}}}{C_s} \quad (2)$$

where S_{geo} represents the geometric surface area of the working electrode and C_s refers to the specific capacitance, which is 0.040 mF cm^{−2} in 1.0 M KOH.³³

The turnover frequency (TOF) could be calculated as follows:

$$\text{TOF} = \frac{j \times A}{4 \times F \times n} \quad (3)$$

$$n = \frac{C_{\text{dl}} \times \Delta V \times A}{2F} \quad (4)$$

where j and A are the geometric current density (A cm^{−2}) and the electrode area (cm²), F is the Faraday constant (C mol^{−1}), n is the active site mole number (mol), and ΔV is the potential range of CV scans (V).

3. Results and discussion

3.1. Synthesis and characterization

As shown in Fig. 1a, the ZnFe–Co₃O₄ nanostructures were synthesized by etching the ZnCo–ZIF precursor, followed by a cation exchange and calcination process. Initially, ZnCo–ZIF hexagonal nanosheets (Fig. S1a) were etched with PA, resulting in the formation of ZnCo–PA nanosheets (Fig. S1b) from Zn²⁺, Co³⁺ and PA molecules. Next, a cation exchange reaction with Fe³⁺ was performed, yielding Fe–ZnCo–PA nanostructures (Fig. S1c). Finally, ZnFe–Co₃O₄ nanostructures were obtained *via* calcination in air for 3 hours (Fig. 1b).

The crystalline structure of the synthesized materials was characterized using XRD. For ZnCo–ZIF, the diffraction peaks shown in Fig. S2a align perfectly with the simulated ZIF–L pattern. Fig. S2b shows the XRD patterns of ZnCo–PA and

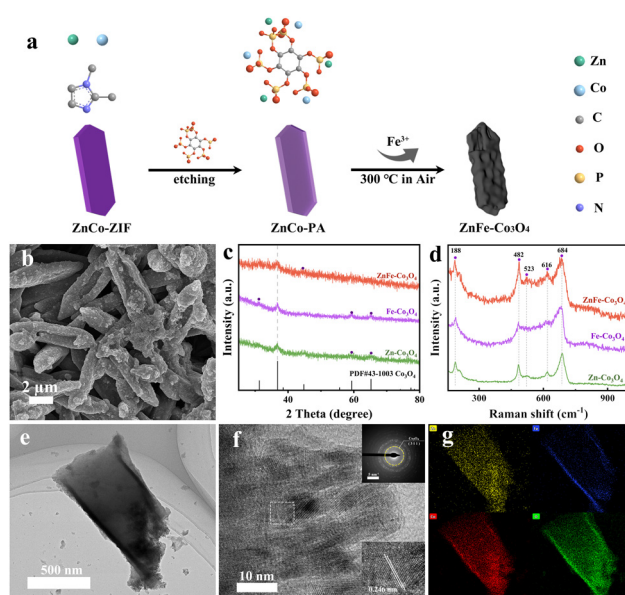


Fig. 1 (a) Schematic illustration of the synthesis of the ZnFe–Co₃O₄; (b) SEM images of ZnFe–Co₃O₄; (c) XRD patterns and (d) Raman spectra of ZnFe–Co₃O₄, Zn–Co₃O₄ and Fe–Co₃O₄; (e) TEM, (f) HRTEM, and (g) elemental mapping images of ZnFe–Co₃O₄. Note that the inset picture in (f) is the SAED image.

Fe–ZnCo–PA, which have no obvious diffraction peaks. Fig. 1c presents the XRD patterns of ZnFe–Co₃O₄, Zn–Co₃O₄ and Fe–Co₃O₄. The results show that the distinct peak located at 36.8° is well indexed to the (311) lattice planes of cubic spinel Co₃O₄, indicating the formation of a spinel structure for the three samples. It is observed that for ZnFe–Co₃O₄, the diffraction peaks located at 59.4° and 65.2° are absent, which can be ascribed to the co-doping of Fe and Zn, which increases the amorphousness. In addition, Fig. S3 observes a negative shift of 0.3° of the ZnFe–Co₃O₄ diffraction peak corresponding to the (311) plane in ZnFe–Co₃O₄, indicating that Zn and Fe are successfully integrated into the Co₃O₄ lattice, causing lattice expansion.

Raman spectroscopy was employed to further verify the structure of ZnFe–Co₃O₄ and the doping of metal atoms. As shown in Fig. 1d, the spectrum exhibits distinct peaks at 188, 482, 523, 616, and 684 cm^{−1}, which are attributable to the F_{2g}, E_g, F_{2g}, F_{2g}, and A_{1g} vibrational modes of Co₃O₄, respectively.³⁴ These observations validate the retention of the spinel structure in ZnFe–Co₃O₄. A comparison with the Raman spectrum of pristine Co₃O₄ (Fig. S4) reveals significant negative shifts in the peaks corresponding to F_{2g} (from 193 to 188 cm^{−1}), F_{2g} (from 622 to 616 cm^{−1}), and A_{1g} (from 690 to 684 cm^{−1}). These shifts further suggest that the incorporation of Zn and Fe induces lattice expansion within the ZnFe–Co₃O₄ structure. Notably, the absence of the 523 cm^{−1} Raman peak in the Fe–Co₃O₄ spectrum may be attributed to changes in the vibrational pattern resulting from the substitution. This substitution likely disrupts the symmetry conditions necessary for the activation of the corresponding vibrational mode, leading to the peak's disappearance.

The microstructure of ZnFe–Co₃O₄ was characterized using a TEM technique. As demonstrated in Fig. 1e, the TEM image reveals that the inside of the electrocatalyst is etched by PA. Fig. 1f presents the high-resolution transmission electron microscopy (HRTEM) image of ZnFe–Co₃O₄, revealing a distinct lattice spacing of 0.246 nm corresponding to the (311) plane of

Co₃O₄. This value exceeds that of the pristine Co₃O₄ lattice fringes (0.243 nm), indicating that the integration of Zn and Fe into the structure results in an expansion of the Co₃O₄ lattice. The crystallographic assignment is further corroborated by selected-area electron diffraction (SAED) analysis (inset image in Fig. 1f). This observation underscores the influence of Zn/Fe doping on the crystal geometry, providing direct visual evidence of lattice distortion due to the doping process. In addition, the EDS mapping results in Fig. 1g indicate the uniform distribution of Zn, Fe, Co, and O atoms within the nanostructure.

Next, XPS was employed to understand the surface chemical valence states and electronic structure of the electrocatalysts. The XPS survey spectrum of ZnFe–Co₃O₄ confirms the presence of Zn, Fe, Co, and O (Fig. S5a).

The high-resolution Co 2p XPS spectrum in Fig. 2a can be deconvoluted into two satellite peaks and four main peaks, corresponding to Co³⁺ (781.0 eV) and Co²⁺ (782.6 eV) of 2p_{3/2}, Co³⁺ (797.0 eV) and Co²⁺ (799.0 eV) of 2p_{1/2}.³⁵ Upon Zn doping, the Co 2p peaks shift negatively by 0.6 eV, while Fe doping induces a positive shift of 0.1 eV. When both Zn and Fe are incorporated, Co 2p peaks shift negatively by 0.5 eV. This change suggests that Zn/Fe co-doping transfers electrons from Zn to Fe and Co, as evidenced by the lower electronegativity of Zn (1.65) compared to Co (1.88) and Fe (1.83) and the susceptibility to electron loss. Additionally, the Co³⁺/Co²⁺ ratio decreases with Zn doping and increases with Fe doping (Fig. S5b), indicating that Zn replaces octahedral Co³⁺ and Fe replaces tetrahedral Co²⁺.³⁶ Next, the changes in electron density around Zn and Fe were explored. As shown in Fig. 2b, the Zn 2p high-resolution spectrum of Zn–Co₃O₄ shows two peaks at 1044.9 eV and 1021.8 eV, which are attributed to 2p_{3/2} and 2p_{1/2} of Zn²⁺, respectively.³⁷ The introduction of Fe results in a positive shift of 0.2 eV in the Zn 2p peaks, implying a decrease in the electronic density around Zn atoms. The Fe 2p high-resolution XPS spectrum of Fe–Co₃O₄ (Fig. 2c) displays four main peaks at 711.4 and 723.6 eV attributed to Fe²⁺, and 714.6 and 726.0 eV attributed to Fe³⁺, respectively.³⁸ Upon Zn

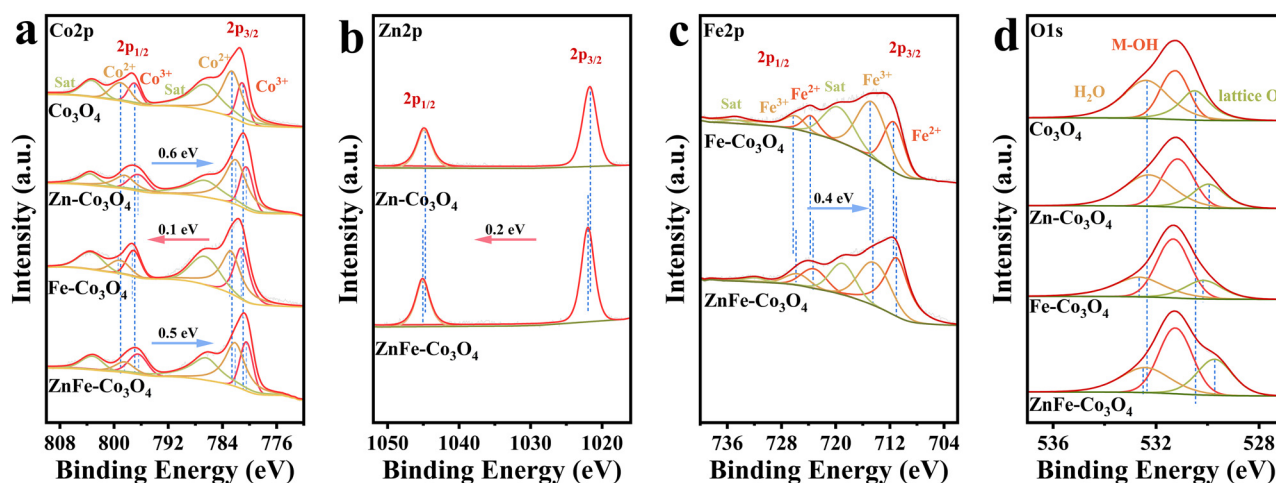


Fig. 2 (a) Co 2p XPS spectra of Co₃O₄, Zn–Co₃O₄, Fe–Co₃O₄ and ZnFe–Co₃O₄; (b) Zn 2p XPS spectra of Zn–Co₃O₄ and ZnFe–Co₃O₄; (c) Fe 2p XPS spectra of Fe–Co₃O₄ and ZnFe–Co₃O₄; (d) O 1s XPS spectra of Co₃O₄, Zn–Co₃O₄, Fe–Co₃O₄ and ZnFe–Co₃O₄.

doping, the Fe 2p peaks shift negatively by 0.4 eV, which indicates an increase in electron density around Fe atoms. Finally, as shown in the high-resolution O 1s XPS spectrum of ZnFe-Co₃O₄ (Fig. 2d), the fitted peaks located at 529.7, 531.2 and 532.4 eV can be attributed to the lattice oxygen, M-OH, and surface H₂O, respectively.^{20,39}

The XPS analysis reveals that doping with Zn and Fe alters the electronic structures of Co₃O₄, affecting the binding energies of Co, Zn, Fe, and O. These shifts provide evidence of the successful incorporation of Zn and Fe into the Co₃O₄ lattice, suggesting changes in the local chemical environments around these dopants.

3.2. Evaluation of alkaline OER performance

The effects of varying Zn and Fe co-doping proportions on the OER electrocatalytic activity of ZnFe-Co₃O₄ were studied preliminarily to optimise OER performance. As can be seen in Fig. S6a–c, the progressive incorporation of Zn and Fe increases the OER activity compared to pristine Co₃O₄ until an optimal dopant threshold is reached. Optimal performance is achieved with an appropriate Zn/Fe ratio and content. Excessive co-doping (e.g., Zn_{0.39}Fe_{0.3}-Co₃O₄) significantly reduces activity, apparently due to lattice distortion or blockage of electrocatalytically active sites. Consequently, the Zn_{0.13}Fe_{0.3}-Co₃O₄ composition (hereafter designated ZnFe-Co₃O₄) is identified as the most OER-active formulation among those investigated.

The OER performance of the ZnFe-Co₃O₄ electrode was evaluated using LSV in a 1.0 M KOH solution. For comparison, the electrocatalytic activities of ZnCo-ZIF, ZnCo-PA, Fe-ZnCo-PA, Zn-Co₃O₄ and Fe-Co₃O₄ were also assessed under identical conditions. As shown in Fig. 3a, the LSV results demonstrate that the ZnFe-Co₃O₄ electrocatalyst outperforms other samples tested in terms of OER performance. Specifically, the overpotentials required to achieve 10 mA cm⁻² and 100 mA cm⁻² are 255 mV and 380 mV for ZnFe-Co₃O₄, respectively, which are significantly lower than Zn-Co₃O₄ (317 mV and 461 mV) and Fe-Co₃O₄ (267 mV and 405 mV) (Fig. 3b), indicating that the co-doping of Zn and Fe atoms effectively enhances the OER performance of the electrocatalyst, respectively. Table S1 lists the OER performance of ZnFe-Co₃O₄ compared with other Co₃O₄-based electrocatalysts reported in the past five years, showing that ZnFe-Co₃O₄ has lower overpotentials at different current densities and demonstrates competitive electrocatalytic performance. Meanwhile, the Tafel slopes of these electrocatalysts were investigated to gain insight into their OER kinetics. As depicted in Fig. 3c, the ZnFe-Co₃O₄ electrocatalyst displays the lowest Tafel slope of 54 mV dec⁻¹ compared with ZnCo-ZIF (128 mV dec⁻¹), ZnCo-PA (110 mV dec⁻¹), Fe-ZnCo-PA (63 mV dec⁻¹), Zn-Co₃O₄ (74 mV dec⁻¹) and Fe-Co₃O₄ (67 mV dec⁻¹), suggesting that ZnFe-Co₃O₄ has fast OER kinetics. The Tafel slope value of ZnFe-Co₃O₄ is between the ideal two-electron coupling (≈ 30 mV dec⁻¹) and the single-electron transfer (≈ 120 mV dec⁻¹), indicating the existence of a partially coupled multi-electron transfer path during the OER process.⁴⁰ But it is not advisable to analyse the electron transfer mechanism only through the Tafel slope, because the Tafel slope

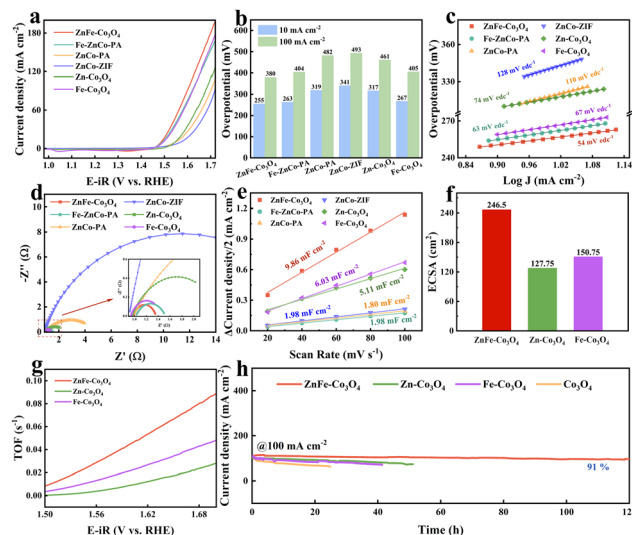


Fig. 3 OER test results: (a) OER voltametric curves; (b) the overpotential comparisons at 10 mA cm⁻² and 100 mA cm⁻²; (c) Tafel slopes; (d) EIS plots; (e) C_{dl} ; (f) ECSA values; (g) TOF values; (h) durability test on the ZnFe-Co₃O₄ with 120 hours at 100 mA cm⁻² in comparison with Zn-Co₃O₄, Fe-Co₃O₄, and pristine Co₃O₄.

will be affected by a variety of factors and there are large fluctuations and changes in values, so we need to combine it with a variety of characterization studies to further verify our conjecture.^{41,42} The EIS analysis reveals that the charge transfer resistance (R_{ct}) of ZnFe-Co₃O₄ is significantly lower than that of the other samples (Fig. 3d). This indicates a faster charge transport process for ZnFe-Co₃O₄. The activity of an electrocatalyst depends on the concentration and intrinsic nature of its active sites. CV measurements were conducted in the non-faradaic region at various sweep rates (Fig. S7) to evaluate the electrochemically active surface area (ECSA) and the number of active sites. As shown in Fig. 3e, ZnFe-Co₃O₄ exhibits the largest double-layer capacitance (C_{dl} , 9.86 mF cm⁻²) value compared to the ZnCo-ZIF (1.98 mF cm⁻²), ZnCo-PA (1.80 mF cm⁻²), Fe-ZnCo-PA (1.98 mF cm⁻²), Zn-Co₃O₄ (5.11 mF cm⁻²) and Fe-Co₃O₄ (6.03 mF cm⁻²). Accordingly, ZnFe-Co₃O₄ exhibits the largest ECSA value (Fig. 3f). TOF is a crucial parameter for evaluating the intrinsic activity of an electrocatalyst. As shown in Fig. 3g, ZnFe-Co₃O₄ exhibits a higher turnover frequency value than Zn-Co₃O₄ and Fe-Co₃O₄, indicating its higher intrinsic activity. Additionally, the long-term stability was assessed at a fixed current density of 100 mA cm⁻² for 120 hours to evaluate the practical application of the electrocatalyst (Fig. 3h). The chronopotentiometry profile reveals that ZnFe-Co₃O₄ exhibits a mere 9% current decay, obviously outperforming Co₃O₄, Zn-Co₃O₄ and Fe-Co₃O₄. Benchmarking against literature data (see Table S2) confirm that ZnFe-Co₃O₄ is one of the most durable Co₃O₄-based catalysts reported to date, corroborating the continuous stabilizing role of Zn/Fe co-doping at elevated current densities.

3.3. Phase transformation and active phase elucidation

To unravel the origins of the superior OER activity of ZnFe-Co₃O₄, the XPS data after the OER stability measurement were

collected. As shown in Fig. 4a, the Co 2p peak shifts negatively and the ratio of $\text{Co}^{3+}/\text{Co}^{2+}$ (2.57) increases after the OER, indicating that more Co^{2+} species were oxidized to Co^{3+} . As expected, the Zn 2p signal disappears after OER durability measurement (Fig. 4b), which suggests that Zn has been leached into the electrolyte. Concurrently, post-OER durability analysis of the electrolyte reveals a significantly higher concentration of Zn than Fe or Co (see Table S3), which definitively confirms Zn's preferential dissolution. This observation is consistent with the findings of Li *et al.*, who previously conducted a systematic exploration of the role of Zn in the oxygen reduction reaction.⁴³ They found that introducing Zn substantially enhances the electrochemical performance. More importantly, breaking the Zn–N bond can stabilise the FeN_4 sites, resulting in a highly stable electrocatalyst. In Fig. 4c, the peak of Fe 2p shifts positively, indicating that the Fe atom was oxidized to a higher valence state after the OER. Additionally, the O 1s XPS spectrum in Fig. 4d reveals negative shifts in the peaks corresponding to lattice oxygen (529.3 eV) and M–OH (531.0 eV), which can be ascribed to the formation of metal (oxy)hydroxide on the surface, resulting in charge transfer and an increase in electron density around the lattice oxygen.^{44,45} It is noted that the $\text{O}_{\text{M-OH}}/\text{O}_{\text{lattice O}}$ ratio in the post-OER electrocatalyst (3.33) is much higher than that in the pristine $\text{ZnFe-Co}_3\text{O}_4$ (1.81). This indicates that the dominant oxygen species are the *OOH species, indicating that surface reconstruction during the OER leads to the formation of active (oxy)hydroxide sites that enhance the OER activity of the electrocatalyst.

Based on the above evidence, we surmise that $\text{ZnFe-Co}_3\text{O}_4$ undergoes an *in situ* reconstitution process that is responsible for its exceptional OER activity and durability. During the initial induction period, the selective leaching of Zn^{2+} creates cation vacancies, which are immediately occupied by migrating Fe^{3+} and Co^{3+} ions. This dynamic redistribution accelerates the

epitaxial growth of a conformal M–OOH (M = Fe or Co) shell, which (i) passivates the underlying spinel lattice against further corrosion and (ii) constitutes the catalytically active phase that is responsible for the sustained, high-rate OER.

To elucidate the correlation between reaction kinetics and electron transfer, *in situ* EIS was conducted by varying the applied potential from 1.20 V to 1.65 V. In the Bode plots, the high-frequency region is associated with the oxidation process of the electrocatalyst, whereas the low-frequency region corresponds to the electron transfer from the electrolyte to the electrocatalytic layer.⁴⁶ More specifically, as shown in Fig. 5a–c, the introduction of Fe effectively reduces the phase angle peak compared with $\text{ZnFe-Co}_3\text{O}_4$, $\text{Fe-Co}_3\text{O}_4$ and $\text{Zn-Co}_3\text{O}_4$, indicating that the incorporation of Fe significantly enhances the electron transfer kinetics.⁴⁷

To understand the OER mechanism over $\text{ZnFe-Co}_3\text{O}_4$, a comprehensive suite of electrochemical experiments was conducted. Unlike the conventional associative electron–proton transfer mechanism (AEM) pathway, the lattice oxygen mechanism (LOM) is characterized by a non-concerted proton–electron transfer process, which exhibits pronounced pH-dependent OER activity.⁴⁸ As shown in Fig. 5d, the current densities increase significantly with pH from 12.5 to 14.0, indicating strong pH dependence on OER activity and suggesting significant non-concerted proton–electron transfer in the OER process. Subsequently, tetramethylammonium (TMA^+) was employed as a chemical probe to detect the presence of negatively charged peroxide/superoxide ($\text{O}_2^{2-}/\text{O}_2^{-}$) intermediates (Fig. 5e). As shown in Fig. 5f, the observed decrease in activity is due to the interaction between TMA^+ and O_2^{2-} species, which hinders the essential O–O coupling for the LOM process.⁴⁹

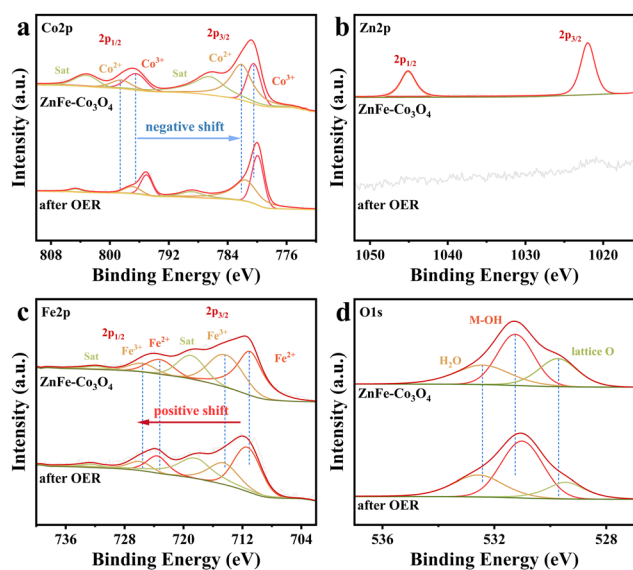


Fig. 4 (a) Co 2p, (b) Zn 2p, (c) Fe 2p and (d) O 1s XPS spectra of $\text{ZnFe-Co}_3\text{O}_4$ collected after OER durability measurement.

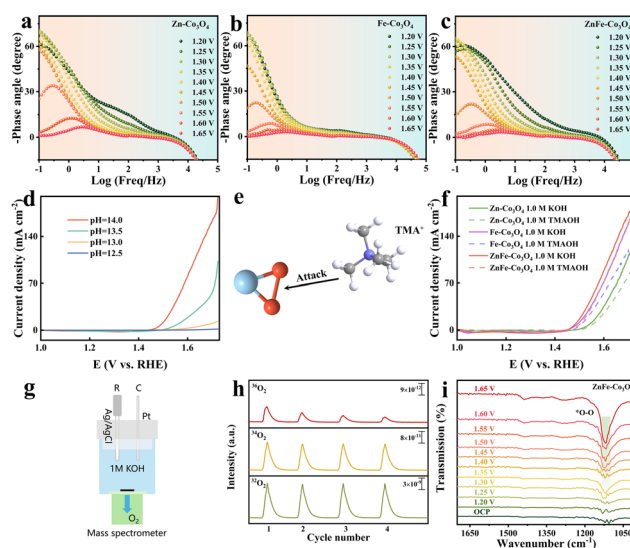


Fig. 5 Bode plots of (a) $\text{Zn-Co}_3\text{O}_4$, (b) $\text{Fe-Co}_3\text{O}_4$ and (c) $\text{ZnFe-Co}_3\text{O}_4$ at different potentials; (d) pH-dependent LSV curves of $\text{ZnFe-Co}_3\text{O}_4$; (e) schematic illustration of the chemical recognition of negatively charged oxygen intermediates by TMA^+ ; (f) polarization curves of $\text{Zn-Co}_3\text{O}_4$, $\text{Fe-Co}_3\text{O}_4$ and $\text{ZnFe-Co}_3\text{O}_4$ in 1.0 M KOH and 1.0 M TMAOH; (g) schematic illustration of DEMS measurement; (h) DEMS spectra of $\text{ZnFe-Co}_3\text{O}_4$ in 1.0 KOH with H_2^{16}O ; and (i) *in situ* ATR-FTIR spectrum of $\text{ZnFe-Co}_3\text{O}_4$.

To directly elucidate the involvement of lattice oxygen in the OER process mediated by the ZnFe-Co₃O₄ electrocatalyst, we conducted ¹⁸O labeling in conjunction with differential electrochemical mass spectroscopy (DEMS) measurements (Fig. 5g). Specifically, we performed four LSV cycles using an ¹⁸O-labeled electrocatalyst within a DEMS electrochemical cell. As depicted in Fig. 5h, the DEMS analysis of the ¹⁸O-labeled ZnFe-Co₃O₄ electrocatalyst reveals pronounced peaks corresponding to the ¹⁸O¹⁶O (*m/z* = 34) species across all four LSV cycles.⁴⁹ These peaks provide unambiguous evidence that lattice oxygen participates in the ZnFe-Co₃O₄ OER process. ³⁶O is formed by the combination of a small amount of the ¹⁸OH group present on the electrocatalyst and lattice oxygen (¹⁸O). To gain further insight into the OER mechanism, *in situ* attenuated total reflectance-Fourier transform infrared (ATR-FTIR) spectroscopy was employed. As illustrated in Fig. 5i, a prominent peak at approximately 1120 cm⁻¹ can be observed in the ZnFe-Co₃O₄ spectrum, which is assigned to the *O-O intermediate,⁵⁰ providing direct spectroscopic evidence that ZnFe-Co₃O₄ follows the LOM during the OER process.

To further understand the origins of the excellent OER activity and stability of ZnFe-Co₃O₄, density functional theory (DFT) calculations were conducted. Fig. S9 shows the theoretical models for ZnFe-Co₃O₄. The electron transfer behaviour of the optimal ZnFe-Co₃O₄ was further studied using electron charge density difference. The calculated charge density results indicate strong electronic interactions between Zn, Fe, and Co. As illustrated in Fig. 6a and b, electrons partially accumulate around the Co and Fe atoms, whereas a significant electron loss is evident around the Zn atom. This electron transfer from Zn, Fe and Co alters the electronic structure of Co, as confirmed by XPS analysis.

To elucidate the mechanistic origin of the OER on ZnFe-Co₃O₄, we subsequently evaluated the Gibbs free-energy profiles of all possible intermediates along both the AEM and LOM. As depicted in Fig. 6c, the AEM and LOM pathways involve fundamentally different elementary steps. The AEM pathway comprises four concerted proton-electron transfer

reactions, resulting in the formation of three intermediates: *OH, *O, and *OOH.⁴⁸ In contrast, the LOM invokes the direct participation of lattice oxygen, enabling O-O bond formation *via* intramolecular coupling and thereby circumventing the linear scaling constraints inherent to the AEM.⁵¹ DFT calculations reveal that the rate-determining step (RDS) on ZnFe-Co₃O₄ exhibits a lower free-energy barrier for the LOM (1.73 eV) than for the AEM (1.76 eV) (Fig. 6d and e). Consequently, the computational data corroborate the preferential operation of the LOM on ZnFe-Co₃O₄ observed experimentally.

To further explore the phase transition of electrocatalyst during the OER, *in situ* Raman spectroscopy was used to observe the overall structural evolution process of various metal-doped Co₃O₄ during electrochemical testing (Fig. 7a-d). Under the open-circuit potential, Co₃O₄, Zn-Co₃O₄, Fe-Co₃O₄ and ZnFe-Co₃O₄ all exhibited characteristic Raman peaks corresponding to the spinel structure of Co₃O₄. As can be seen in Fig. 7a, until 1.50 V, the Raman peaks of pure Co₃O₄ all disappeared, and no new characteristic peaks appeared as the potential increased. This suggests that the Co₃O₄ structure completely reconstructs or dissolves during the OER. In contrast, the *in situ* Raman spectra of Zn-Co₃O₄ (Fig. 7b) revealed that the intensity of the Co₃O₄ spinel characteristic peaks decreased progressively with an increase in potential.

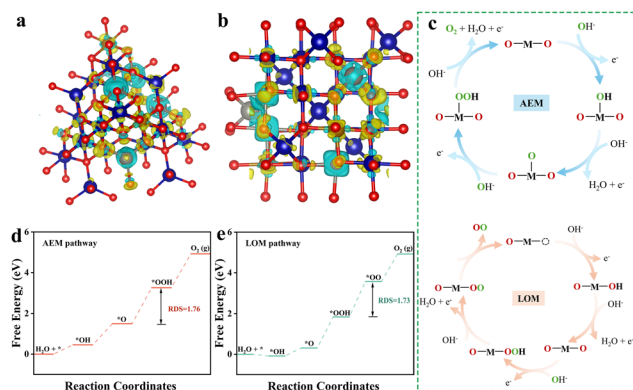


Fig. 6 (a) and (b) Differential charge density of ZnFe-Co₃O₄; yellow and blue lines represent the electron accumulation and depletion; (c) schematic illustration of the AEM and LOM toward the alkaline OER; panels are Gibbs free-energy diagrams of (d) AEM and (e) LOM pathways.

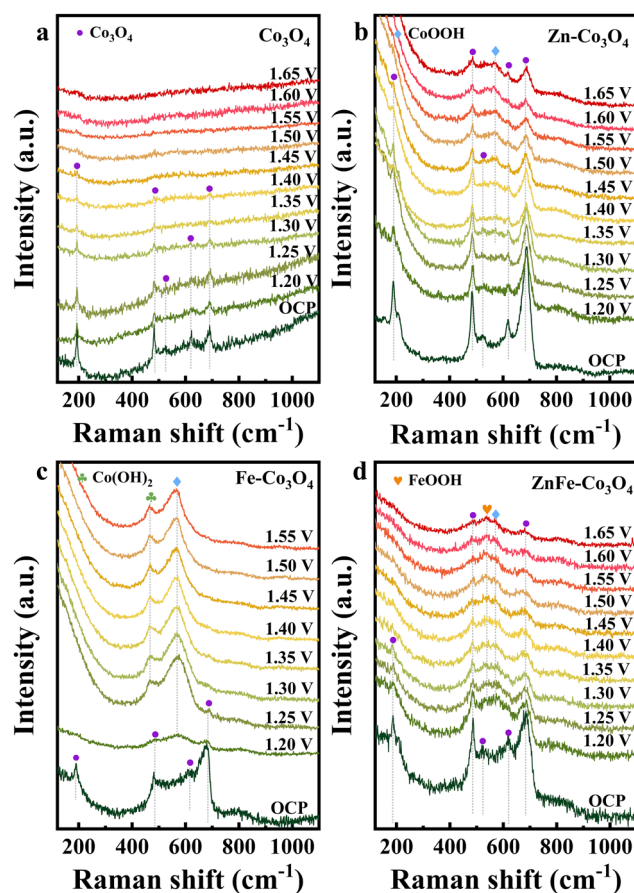


Fig. 7 *In situ* Raman spectroscopy of (a) Co₃O₄, (b) Zn-Co₃O₄, (c) Fe-Co₃O₄ and (d) ZnFe-Co₃O₄.

Interestingly, a new peak appeared at 566 cm^{-1} from 1.30 V, which can be attributed to the formation of CoOOH.⁵² This indicates that Zn doping stabilizes the Co_3O_4 structure to some extent. In contrast, the *in situ* Raman spectra of Fe- Co_3O_4 (Fig. 7c) shows that the Raman characteristic peaks attributed to the Co_3O_4 spinel structure at 1.30 V completely disappear and that the characteristic peaks of $\text{Co}(\text{OH})_2$ and CoOOH appear at 465 and 565 cm^{-1} .⁵³ This suggests that Fe doping promotes a more rapid transformation of Co_3O_4 to (oxy)hydroxide species during the OER process. The *in situ* Raman spectra of ZnFe- Co_3O_4 (Fig. 7d) showed that peaks attributed to FeOOH (537 cm^{-1}) and CoOOH (566 cm^{-1}) appeared at a potential of 1.25 V.^{54,55} Remarkably, even at 1.65 V, some characteristic peaks of the Co_3O_4 spinel structure (486 and 684 cm^{-1}) were still present. This indicates that ZnFe- Co_3O_4 also undergoes partial structural transformation during the OER, with the formation of highly active FeOOH/CoOOH species on the surface. Meanwhile, compared with the *in situ* Raman spectra of Fe- Co_3O_4 , the introduction of Zn atoms promoted the formation of FeOOH, which further proved the coordinated effect of Zn and Fe atom co-doping in ZnFe- Co_3O_4 .

Based on these observations, ZnFe- Co_3O_4 follows the LOM in the OER process, and its superior OER performance of ZnFe- Co_3O_4 is mainly attributed to the formation of highly reactive FeOOH/CoOOH species by the surface reconstruction during the OER. By comparing the *in situ* Raman spectra of different metal-doped Co_3O_4 electrocatalysts, it is evident that Zn enhances the stability of Co_3O_4 , allowing for surface reconstruction without complete phase transitions, while Fe facilitates the generation of highly active (oxy)hydroxide species. This synergistic effect between Zn and Fe doping significantly improves the electrocatalytic activity and stability of ZnFe- Co_3O_4 for the OER.

4. Conclusion

In summary, this study successfully synthesized a Zn/Fe co-doped Co_3O_4 nanostructure (ZnFe- Co_3O_4) using a ZIF precursor combined with phytic acid etching and heteroatom doping strategies. The resulting electrocatalyst exhibited remarkable performance for the OER in alkaline media, with low overpotentials of 255 mV at 10 mA cm^{-2} , a Tafel slope of 54 mV dec^{-1} and excellent long-term durability for up to 120 hours at 100 mA cm^{-2} . Comprehensive characterization and electrochemical measurement reveal that the superior OER performance of ZnFe- Co_3O_4 is attributed to the synergistic effects of Zn and Fe atom doping. Specifically, Zn atoms stabilize the Co_3O_4 structure, allowing for surface reconstruction without complete phase transitions, while Fe atoms promote the formation of highly active (oxy)hydroxide species (*i.e.*, FeOOH/CoOOH) during the OER process. DFT, DEMS, *in situ* ATR-FTIR and various other techniques collectively demonstrate that ZnFe- Co_3O_4 follows the LOM pathway. The findings highlight the importance of synergistic doping and surface reconstruction in optimizing the electrocatalytic properties of Co_3O_4 -based materials, paving the way for the development of more efficient and durable OER electrocatalysts.

Author contributions

Qianwen Chen: experimental design, data acquisition, and writing – review & editing. Yanbing Huang: writing – review & editing. Wanshun Duan: data acquisition. Qijia Su: data acquisition. Yilong Wang: writing – review & editing. Fuxi Bao: funding acquisition, supervision and writing – review & editing. Junjun Zhang: writing – review & editing. Wen Gu: funding acquisition, supervision and writing – review & editing.

Conflicts of interest

The authors declare that they have no known competing financial interests or personal relationships that could have appeared to influence the work reported in this paper.

Data availability

All data supporting this study are included in the article and its SI. The authors or corresponding authors shall provide all the original data upon reasonable request.

Supplementary information available: The supplemental information file contains experimental details and descriptions of *in situ* characterization. In addition, supplemental data results such as ICP-OES, SEM, XRD, Raman, XPS and DFT are included. See DOI: <https://doi.org/10.1039/d5mh01137j>

Acknowledgements

The authors would like to acknowledge the financial support from the Tianchi Elite Talent Program, the National Talent Plan Program (No. CZ002712 and No. KZ6009), the High-level Talents Projects of Shihezi University (RCZK202324), and the Bingtuan Science and Technology Program (No. 2023AB033). The authors would also be grateful to the Shiyanjia Lab (www.shiyanjia.com) for the XPS tests and the characterization support provided by the multi-scale environmental control nanocatalysis synthesis and characterization platform of Shihezi University.

Notes and references

- 1 E. Aramendia, P. E. Brockway, P. G. Taylor, J. B. Norman, M. K. Heun and Z. Marshall, *Nat. Energy*, 2024, **9**, 803–816.
- 2 Z. Li, S. Fang, H. Sun, R. J. Chung, X. Fang and J. H. He, *Adv. Energy Mater.*, 2023, **13**, 2203019.
- 3 H. Song, S. Luo, H. Huang, B. Deng and J. Ye, *ACS Energy Lett.*, 2022, **7**, 1043–1065.
- 4 Z. Yang, H. Liu, Y. Yuan and M. Li, *Energy*, 2024, **304**, 132160.
- 5 A. J. Shih, M. C. O. Monteiro, F. Dattila, D. Pavesi, M. Philips, A. H. M. da Silva, R. E. Vos, K. Ojha, S. Park, O. van der Heijden, G. Marcandalli, A. Goyal, M. Villalba, X. Chen, G. T. K. K. Gunasooriya, I. McCrum, R. Mom, N. López and M. T. M. Koper, *Nat. Rev. Methods Primers*, 2022, **2**, 84.

- 6 B. Zhai, J. Zeng, Y. Wang, P. Niu, S. Wang and L. Li, *Appl. Catal., B*, 2024, **359**, 124496.
- 7 X. Wang, H. Zhong, S. Xi, W. S. V. Lee and J. Xue, *Adv. Mater.*, 2022, **34**, 2107956.
- 8 H. Zhong, Q. Zhang, J. Yu, X. Zhang, C. Wu, Y. Ma, H. An, H. Wang, J. Zhang, X. Wang and J. Xue, *Adv. Energy Mater.*, 2023, **13**, 2301391.
- 9 X. Xie, L. Du, L. Yan, S. Park, Y. Qiu, J. Sokolowski, W. Wang and Y. Shao, *Adv. Funct. Mater.*, 2022, **32**, 2110036.
- 10 H. Li, W. Wang, S. Xue, J. He, C. Liu, G. Gao, S. Di, S. Wang, J. Wang, Z. Yu and L. Li, *J. Am. Chem. Soc.*, 2024, **146**, 9124–9133.
- 11 F.-Y. Chen, Z.-Y. Wu, Z. Adler and H. Wang, *Joule*, 2021, **5**, 1704–1731.
- 12 H. Kim, T. Y. Yoo, M. S. Bootharaju, J. H. Kim, D. Y. Chung and T. Hyeon, *Adv. Sci.*, 2021, **9**, 2104054.
- 13 Z. P. Wu, X. F. Lu, S. Q. Zang and X. W. Lou, *Adv. Funct. Mater.*, 2020, **30**, 1910274.
- 14 M. Yu, E. Budiyo and H. Tüysüz, *Angew. Chem., Int. Ed.*, 2021, **61**, e202103824.
- 15 K. Zhang and R. Zou, *Small*, 2021, **17**, 2100129.
- 16 Z. Liang, D. Shen, L. Wang and H. Fu, *Nano Res.*, 2023, **17**, 2234–2269.
- 17 C. He, L. Yang, J. Wang, T. Wang, J. Ju, Y. Lu and W. Chen, *Carbon Energy*, 2024, **6**, e573.
- 18 M. Sun, R. Ge, S. Li, L. Dai, Y. Li, B. Liu and W. Li, *J. Energy Chem.*, 2024, **91**, 453–474.
- 19 Y. Peng, H. Hajiyani and R. Pentcheva, *ACS Catal.*, 2021, **11**, 5601–5613.
- 20 K. Lu, T. Gu, L. Zhang, Z. Wu, R. Wang and X. Li, *Chem. Eng. J.*, 2021, **408**, 127352.
- 21 Y. Huang, M. Li, F. Pan, Z. Zhu, H. Sun, Y. Tang and G. Fu, *Carbon Energy*, 2022, **5**, e279.
- 22 A. Shahzad, F. Zulfiqar and M. Arif Nadeem, *Coord. Chem. Rev.*, 2023, **477**, 214925.
- 23 P. Zhao, S. Fu, L. Cheng, Z. Jiao and M. Wu, *Coord. Chem. Rev.*, 2024, **498**, 215452.
- 24 J. Liu, D. Zhu, C. Guo, A. Vasileff and S. Z. Qiao, *Adv. Energy Mater.*, 2017, **7**, 1700518.
- 25 H. S. Jadhav, H. A. Bandal, S. Ramakrishna and H. Kim, *Adv. Mater.*, 2022, **34**, 2107072.
- 26 A. Radwan, H. Jin, D. He and S. Mu, *Nano-Micro Lett.*, 2021, **13**, 1–32.
- 27 Y. Hua, X. Li, C. Chen and H. Pang, *Chem. Eng. J.*, 2019, **370**, 37–59.
- 28 C. Gao, S. Mu, R. Yan, F. Chen, T. Ma, S. Cao, S. Li, L. Ma, Y. Wang and C. Cheng, *Small*, 2022, **18**, 2105409.
- 29 J. Zhang, D. Wu, L. Cai, Y. Lu, F. Cheng, L. Shi, Q. Yi, Y. Liu and Y. Huang, *J. Energy Chem.*, 2025, **100**, 226–233.
- 30 Y. Yao, S. Chen, Z. Wang, J. Xu, J. Chen and Y. Li, *ACS Appl. Nano Mater.*, 2024, **7**, 22130–22136.
- 31 Q. Chen, M. Yao, Y. Zhou, Y. Sun, G. Zhang and H. Pang, *Coord. Chem. Rev.*, 2024, **517**, 216016.
- 32 C.-J. Huang, H.-M. Xu, T.-Y. Shuai, Q.-N. Zhan, Z.-J. Zhang and G.-R. Li, *Appl. Catal., B*, 2023, **325**, 122313.
- 33 H. Chen, S. Qiao, J. Yang and X. Du, *Mol. Catal.*, 2022, **518**, 112086.
- 34 L. Xia, L. Bo, W. Shi, Y. Zhang, Y. Shen, X. Ji, X. Guan, Y. Wang and J. Tong, *Chem. Eng. J.*, 2023, **452**, 139250.
- 35 A. Wang, W. Wang, J. Xu, A. Zhu, C. Zhao, M. Yu, G. Shi, J. Yan, S. Sun and W. Wang, *Adv. Energy Mater.*, 2023, **13**, 2302537.
- 36 G. Zhang, J. Pei, Y. Wang, G. Wang, Y. Wang, W. Liu, J. Xu, P. An, H. Huang, L. Zheng, S. Chu, J. Dong and J. Zhang, *Angew. Chem., Int. Ed.*, 2024, **63**, e202407509.
- 37 B. Zhang, Y. Luo, D. Xiang, J. Qin, K. Miao, X. Wang, X. Kang and Y. Tian, *Adv. Funct. Mater.*, 2023, **33**, 2214529.
- 38 Y. Zhang, W. Zhang, X. Zhang, J. Li and G. Liu, *J. Energy Chem.*, 2025, **101**, 676–684.
- 39 C. Jia, X. Xiang, J. Zhang, Z. He, Z. Gong, H. Chen, N. Zhang, X. Wang, S. Zhao and Y. Chen, *Adv. Funct. Mater.*, 2023, **33**, 2301981.
- 40 O. van der Heijden, S. Park, R. E. Vos, J. J. J. Eggebeen and M. T. M. Koper, *ACS Energy Lett.*, 2024, **9**, 1871–1879.
- 41 R. D. L. Smith, C. Pasquini, S. Loos, P. Chernev, K. Klingan, P. Kubella, M. R. Mohammadi, D. Gonzalez-Flores and H. Dau, *Nat. Commun.*, 2017, **8**, 2022.
- 42 O. van der Heijden, R. E. Vos and M. T. M. Koper, *ACS Energy Lett.*, 2025, **10**, 3040–3049.
- 43 H. Li, S. Di, P. Niu, S. Wang, J. Wang and L. Li, *Energy Environ. Sci.*, 2022, **15**, 1601–1610.
- 44 D. Liu, H. Ai, J. Li, M. Fang, M. Chen, D. Liu, X. Du, P. Zhou, F. Li, K. H. Lo, Y. Tang, S. Chen, L. Wang, G. Xing and H. Pan, *Adv. Energy Mater.*, 2020, **10**, 2002464.
- 45 Y. Li, Y. Wu, H. Hao, M. Yuan, Z. Lv, L. Xu and B. Wei, *Appl. Catal., B*, 2022, **305**, 121033.
- 46 Q. Quan, Y. Zhang, H. Li, W. Wang, P. Xie, D. Chen, W. Wang, Y. Meng, D. Yin, Y. Li, D. Song, L. Chen, S. Li, C. Yang, T. Yanagida, C.-Y. Wong, S. Yip and J. C. Ho, *Nat. Commun.*, 2025, **16**, 2908.
- 47 Y. Huang, Z. Gu, J. Wang, H. Zhang, C. Sun, H. Xie, A. Kong, W. Guo, J. Liu and F. Bao, *Appl. Catal., B*, 2025, **371**, 125221.
- 48 S. Guan, B. Xu, X. Yu, Y. Ye, Y. Liu, T. Guan, Y. Yang, J. Gao, K. Li and J. Wang, *ACS Catal.*, 2024, **14**, 17806–17817.
- 49 T. Zhang, H.-F. Zhao, Z.-J. Chen, Q. Yang, N. Gao, L. Li, N. Luo, J. Zheng, S.-D. Bao, J. Peng, X. Peng, X.-W. Liu and H.-B. Yu, *Nat. Commun.*, 2025, **16**, 3327.
- 50 L. Wang, S.-F. Hung, S. Zhao, Y. Wang, S. Bi, S. Li, J.-J. Ma, C. Zhang, Y. Zhang, L. Li, T.-Y. Chen, H.-Y. Chen, F. Hu, Y. Wu and S. Peng, *Nat. Commun.*, 2025, **16**, 3502.
- 51 X. Luo, H. Zhao, X. Tan, S. Lin, K. Yu, X. Mu, Z. Tao, P. Ji and S. Mu, *Nat. Commun.*, 2024, **15**, 8293.
- 52 Y. Li, X. Zhang and Z. Zheng, *Small*, 2022, **18**, e2107594.
- 53 Z. Huang, Z. Wang, H. Rabl, S. Naghdi, Q. Zhou, S. Schwarz, D. H. Apaydin, Y. Yu and D. Eder, *Nat. Commun.*, 2024, **15**, 1–14.
- 54 J. Hu, J. Yin, A. Peng, D. Zeng, J. Ke, J. Liu and K. Guo, *Small*, 2024, **20**, 2402881.
- 55 X. Zhou, J. Zhang, M. Zhang, X. Du, W. Bao, J. Han, X. Lin, P. Zhang and Z. Luo, *Inorg. Chem. Front.*, 2025, DOI: [10.1039/d5qi00418g](https://doi.org/10.1039/d5qi00418g).